Three-band, 1.9-μm axial resolution full-field optical coherence microscopy over a 530–1700 nm wavelength range using a single camera

Antoine Federici* and Arnaud Dubois

Laboratoire Charles Fabry, CNRS UMR 8501, Institut d'Optique Graduate School, Univ. Paris-Sud, 2 avenue Augustin Fresnel, 91127 Palaiseau cedex, France

**Corresponding author: antoine.federici@institutoptique.fr*

Received November 8, 2013; revised January 17, 2014; accepted January 22, 2014; posted January 24, 2014 (Doc. ID 200987); published March 5, 2014

Full-field optical coherence microscopy is an established optical technology based on low-coherence interference microscopy for high-resolution imaging of semitransparent samples. In this Letter, we demonstrate an extension of the technique using a visible to short-wavelength infrared camera and a halogen lamp to image in three distinct bands centered at 635, 870, and 1170 nm. Reflective microscope objectives are employed to minimize chromatic aberrations of the imaging system operating over a spectral range extending from 530 to 1700 nm. Constant 1.9-μm axial resolution (measured in air) is achieved in each of the three bands. A dynamic dispersion compensation system is set up to preserve the axial resolution when the imaging depth is varied. The images can be analyzed in the conventional RGB color channels representation to generate three-dimensional images with enhanced contrast. The capability of the system is illustrated by imaging different samples.

OCIS codes: (170.4500) Optical coherence tomography; (170.6510) Spectroscopy, tissue diagnostics; (110.4234) Multispectral and hyperspectral imaging; (180.6900) Three-dimensional microscopy; (180.3170) Interference microscopy.
http://dx.doi.org/10.1364/OL.39.001374

Full-field optical coherence microscopy (FF-OCM), also often referred to as full-field optical coherence tomography (OCT), was introduced a few years ago as an alternative to conventional OCT. FF-OCM uses an interference microscope and an area camera combined with a low coherence illumination source for acquisition of *en face* tomographic images without transverse scanning [1,2]. The technique was applied to high-resolution (reaching ∼0.9 μm at ∼700 nm center wavelength [3]) noninvasive three-dimensional imaging of various semitransparent samples.

Several extensions of conventional FF-OCM have been developed, including the ability to exploit the spectroscopic response of the imaged sample. The purpose of this complementary imaging modality is to enhance image contrast, permitting better differentiation of the sample structures through their spectroscopic properties and providing additional information on the sample composition. A first technological approach involves detecting the whole interferometric signal and analyzing it using Fourier mathematics to provide spatially resolved spectroscopic information [4]. However, this method requires intensive computation and high mechanical stability to avoid degradation of phase-sensitive information. When implemented to conventional scanning OCT [5], this method is much faster, but implies a trade-off between spectral resolution and spatial resolution. This concern can be overcome in *en face* imaging by using high NA objectives for confocal sectioning as demonstrated in spectral-domain OCT (SD-OCT) [6]. Nevertheless, the working distance may then be a limitation of the accessible imaging depth.

An alternative to take advantage of the spectroscopic response of the sample is to image it in several distinct bands. High-resolution FF-OCM [7] and conventional OCT [8] were demonstrated in two bands, at ∼800 nm and ∼1200 nm center wavelengths, using, respectively, a halogen lamp and a supercontinuum laser as broadband light sources and two different detectors. Even though imaging can be performed simultaneously in the two bands, these approaches are not technologically convenient for multiband imaging since each band requires a dedicated detector. Three-band FF-OCM, using a single camera and three distinct light-emitting diodes (LEDs) in the red (R), green (G) and blue (B) bands, was reported to produce true-color images [9]. However, this system has a moderate axial resolution of ∼10 μm due to the relatively narrow power spectrum of LEDs. Besides, the spectral range is limited to the visible, which is not optimal for deep imaging. Three-band imaging was also implemented in SD-OCT, at high speed and high spatial resolution, but over a spectral range limited to ∼40 nm [6].

Three-band imaging is particularly interesting to produce color images using the conventional RGB three color channels. For high-resolution three-band FF-OCM, the bands have to be broad and possibly in the infrared to enable deep imaging, which constitutes a technological challenge. In this Letter, we report on a high-resolution high-sensitivity three-band FF-OCM system using a single camera and a single light source, covering a spectral range from 530 to 1700 nm.

The layout of our three-band FF-OCM imaging system is depicted in Fig. 1. A halogen lamp is used as the low-coherence light source. It is set up in a Köhler illumination arrangement to achieve uniform illumination of the sample. A broadband beam splitter separates the light beam into a reference arm and a sample arm of a Linnik-type interferometer with a microscope objective placed in each arm [10]. One surface of a wedge prism made of BK7 glass is used to provide a plane reference surface with 4% reflectivity, which is placed in the focal plane of the microscope objective in the reference arm. The angle of the wedge prism prevents the light reflected

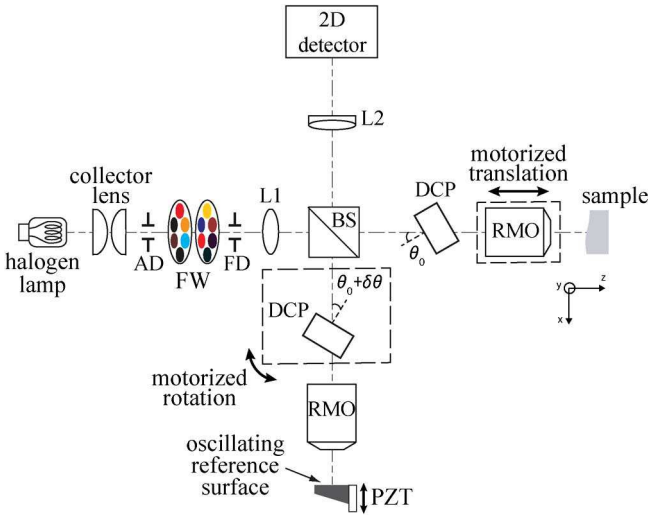

Fig. 1. Experimental achromatic setup. AD, aperture diaphragm; FD, field diaphragm; BS, beam splitter; DCP, dispersion compensation plate; RMO, reflective microscope objective; PZT, piezoelectric transducer; L1, lens; L2, tube lenses (doublets); FW, filter wheels.

by the opposite surface from being collected by the microscope objective. The sample is placed in the other arm of the interferometer under an identical microscope objective. The optical path length of the reference arm is adjusted by rotating a 12-mm thick fused silica glass plate placed in the reference arm, using a motorized rotation stage. Another identical glass plate is placed at a fixed angle in the sample arm to compensate for the dispersion mismatch introduced by the other plate. The zero-delay position can thus be varied to get *en face* tomographic images at different depths in the sample, while compensating the dispersion mismatch as will be explained later. The microscope objective in the sample arm is mounted on a linear motorized translation stage and is moved appropriately to focus the imaging plane. Dynamic focusing is thus achieved as the imaging depth is varied [11].

The interferometric images are projected onto the area sensor of a camera (OWL SW1.7-CL-HSVIS-SWIR manufactured by Raptor Photonics) based on InGaAs technology. The camera has an extended sensitivity in the visible to offer a spectral sensitivity ranging from 400 to 1700 nm [see Fig. 2(a)]. The pixel resolution is 320×256, with a pixel pitch of 30 μm × 30 μm. The frame rate can be set up to 346 Hz. *En face* oriented tomographic images are obtained by arithmetic combination

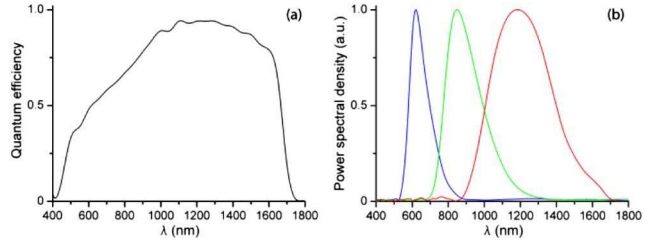

Fig. 2. (a) Camera, quantum efficiency (in electron/photons) provided by the manufacturer. (b) Experimental power spectral densities of the three bands (blue = band 1, green = band 2, red = band 3).

of four phase-shifted interferometric images [10]. The phase-shift is generated by making the reference surface oscillate using a piezoelectric transducer synchronized with the camera triggering signal.

Two different 400-mm focal length doublet lenses, one optimized for the 600–1000 nm wavelength range and the other one for 1000–1600 nm, are used depending on the filter combination, to project the interferometric images onto the camera sensor. Kinematic bases are employed for interchanging the lenses quickly and ensuring that still exactly the same part of the sample is imaged.

Three illumination bands [see Fig. 2(b)] within the range of spectral sensitivity of the camera are selected by using three filter sets holded in filter wheels (see Table 1). The three bands, centered at 635, 870 and 1170 nm, spread out over the 530–1700 nm spectral range. Changing the filter set and the tube lens takes only a few seconds. Nevertheless, this requires the sample to be stable during this time, which may prevent from *in vivo* biomedical imaging.

Water-immersion microscope objectives typically cannot be used to image at wavelengths longer than ~1.3 μm, because of the absorption of light by water. Besides, refractive objectives cannot function efficiently over the broad spectral range considered here (530–1700 nm) because of optical aberrations and limited transmittance. Instead, reflective microscope objectives are used here (15×, 0.28NA), which are reverse Cassegrains following the Schwarzschild design. The primary mirror has a spherical concave surface with a center hole. The secondary mirror is a small convex spherical mirror that is machined into a spider assembly. The mirrors are broadband coated with gold for optimal reflectivity from visible to infrared. Accordingly, they have zero chromatic aberration, and negligible coma, spherical, and astigmatic aberrations.

Due to the broad spectra considered here, dispersion mismatch between the two arms of the interferometer may lead to a significant decrease of signal contrast and axial resolution. This phenomenon is partially avoided thanks to the rotating glass plate placed in the reference arm, whose role is to adjust the zero-delay position as well as to keep the dispersion mismatch minimized as the imaging depth in the sample is changed. Theoretically, a perfect compensation is achieved if the group velocity dispersion of the glass plate is equal to the one of the sample. By assuming that biological samples are mainly made of water, fused silica appears well suited with regard to its dispersion properties [12]. Both dispersion compensation plates (DCPs) are initially oriented at the same angle θ_0 (see Fig. 1). According to numerical simulations, $\theta_0 = 30°$ appears to be a good trade-off for minimizing both the deviation of the light beam and the losses by reflection on the DCP surfaces when the plate is rotated by an additional angle $\delta\theta$. This value is then chosen as fixed angle for the DCP in the sample arm and as starting angle for the reference DCP rotation. For the three bands, we measured the variation of the optical path length difference, called d, with respect to $\delta\theta$ and fitted it with a polynomial function of order 3 (Fig. 3) in order to set the rotating movement parameters of the reference DCP during the acquisition. The experimental data differ by less than 1% with

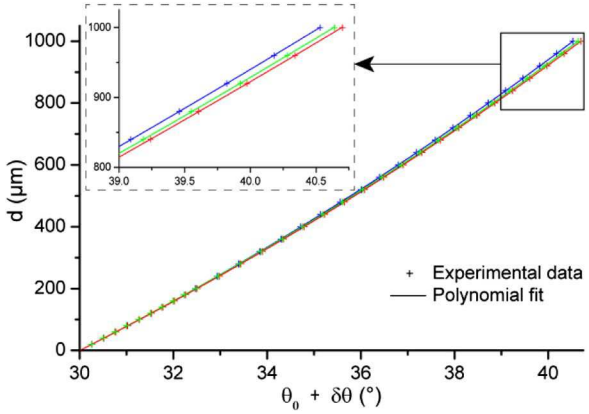

Fig. 3. Evolution of the optical path length difference d, with respect to $\delta\theta$ in band 1 (blue), band 2 (green), and band 3 (red). Experimental data and polynomial fits are displayed.

theoretical predictions for a rotation angle $\delta\theta$ up to 10° corresponding to $d \sim 1$ mm. Due to optical dispersion in the DCPs, the value of d varies by 2% for $\delta\theta \sim 10°$ depending on the band (see inset in Fig. 3).

Similarly, when imaging deeply into a sample, a shift of the imaging depth is observed depending on the band because of dispersion in the sample. These phenomena are corrected by appropriate axial linear dilatation of the image in the three bands. This procedure, based on image correlation analysis, is required for superposition of the three acquired images resulting in a single RGB image.

The interferometric signal, measured in the three bands using a mirror as a sample, is shown together with its envelope in Fig. 4. Fourier analysis of these data provides the power spectral densities displayed in Fig. 2(b).

Without dispersion mismatch, the axial resolution of the imaging system, Δz, depends on the mean wavelength λ_0 and the width $\Delta\lambda$ of the effective power spectrum [7]. The larger the mean wavelength, the broader the spectrum must be to keep Δz constant. The width of each of the three spectral bands is adjusted so that the axial resolution Δz is quasi-constant over the three imaging bands. The axial resolution, defined as the FWHM of the fringe envelope, was then measured to be ~1.9 μm.

Unlike the axial resolution, the transverse resolution $\Delta(x, y)$ is essentially determined by the NA of the microscope objectives and the mean wavelength λ_0. The transverse resolution was measured in the three bands by imaging 0.1-μm diameter gold beads embedded in an agarose gel. The results are shown in Table 1.

Experimental values are similar to theoretical ones and confirm the expected differences between the transverse resolutions in the three bands. Like the axial

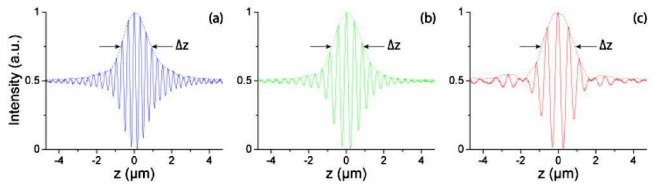

Fig. 4. Interferograms measured in (a) band 1, (b) band 2, and (c) band 3.

Table 1. Features and Experimental Performances in the Three Bands

	Band 1	Band 2	Band 3
Filter Combination	OG590, KG1, KG3, KG5	RG780, RG9, KG1	FEL0950, BG36, DMSP1500
λ_0 (nm)	635	870	1170
$\Delta\lambda$ (nm)	120	220	390
Δz (μm)	1.9	1.9	1.9
$\Delta(x, y)^a$ (μm)	2.4	2.4	2.4
$\Delta(x, y)$ (μm)	1.4	1.9	2.4

[a]After post-acquisition image convolution.

resolution, it is desirable to have the same transverse resolution in the three imaging bands for superposition of the images. The acquired data are then processed by convolving every *en face* image with a suited two-dimensional Gaussian function, so that the transverse resolution is constant over the three bands.

The FF-OCM signal is proportional to the square root of the sample reflectivity and to the number N of interferometric images that are accumulated. In order to achieve identical signals in the three bands for a sample with spectrally constant reflectivity, we first adjust the exposure time of the camera depending on the band so that the number of photoelectrons is always close to the full-well capacity, and then set N depending on the band to compensate for variation of the fringe contrast. This provides a detection of reflectivity variations with a precision of ~10%. By using a BK7 glass plate whose reflectivity varies by less than 5% between the bands, we choose N equals to 30 (band 1), 26 (band 2), and 24 (band 3) to obtain a quasi-constant FF-OCM signal over the three bands given the precision. In these conditions, the acquisition frame rate of *en face* tomographic images varies from 1 Hz in band 1 to 4 Hz in band 3, while the detection sensitivity defined as the lowest detectable sample reflectivity [10] is close to 85 dB for the three bands. Thus, for each band, the performances are comparable to the ones of conventional FF-OCM [1,3,11].

Three-band imaging can reveal the presence of details in a sample, owing to their wavelength-dependent scattering and absorption properties, which are imperceptible otherwise. As an illustration of the system ability, a wood sample with two drops of different pigment colors deposited at its surface was imaged (Fig. 5). Since the reflectivity of wood structures does not vary significantly in the three bands, the surface of the sample appears white. Red stains are visible on the surface in the RGB representation due to sidelobes in the interferogram envelop of band 3 [Fig. 4(c)]. A slight red hue can also be observed on the wood layers. This tendency is consistent with the fact that longer wavelengths penetrate deeper than shorter wavelengths due to reduced scattering [4,5]. One can notice that while it is almost impossible to simultaneously detect and distinguish the two painted regions with only one or two bands, three-band imaging with RGB representation clearly reveals them. Intensity profiles of the RGB image are shown to highlight the presence of these two pigments and provide a measurement of their size. One can deduce from Fig. 5 that one of the pigment absorbs light between 600 and 1000 nm

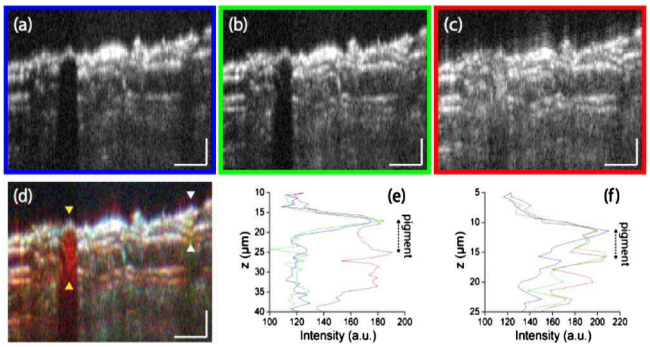

Fig. 5. xz sections of a partially painted wood sample with Prussian blue and Cerulean blue oil paintings in (a) band 1, (b) band, 2, (c) band 3, and (d) with RGB representation. (e), (f) Cuts along the z axis of the RGB image intensity at the pigment locations. The positions of the cuts are indicated by yellow (e), and white (f) arrows in the RGB image (d). The scale bar is 50 μm along the x axis and 10 μm along the z axis.

(band 1 and 2) and appears red in the RGB image, whereas the other pigment absorbs the visible (band 1) and infrared light beyond ~1.3 μm (part of band 3) and then appears greenish in the RGB representation. This is consistent with the spectroscopic properties of the Prussian blue and Cerulean blue oil paintings [13].

An example of how three-band FF-OCM can be used for biological sample characterization is shown in Fig. 6. Two distinct human hairs, a light one and a dark one, were imaged.

Hair darkness is relative to the quantity of eumelanin pigments. Since eumelanin absorption decreases as wavelength increases [14], dark hair absorbs visible light, but not infrared light, much more readily than light hair. This is why a difference of imaging penetration depth can be observed between the hairs in band 1 but not in band 3. Scattering reinforces this difference since it is weaker in the infrared and thus the imaging penetration depth is less limited. However, signal penetration here is dominated by absorption since the difference between absorption coefficients is much more important than between scattering coefficients for distinct eumelanin in concentrations [14]. Three-band imaging can thus reveal spectral absorption properties of samples. One can notice that the sections of the hairs do not appear circular in the images. This artifact comes from a distortion of the optical wavefront due to the curved shape of the upper interface between the sample and air, and to the inhomogeneity of the refractive index within the sample.

This Letter presents an achromatic FF-OCM setup capable of high-resolution three-band imaging over a wavelength range from 530 to 1700 nm. Great care was taken to reach similar performances over the three bands. The system has a constant axial resolution of ~1.9 μm and a transverse resolution of 2.4 μm. Detection sensitivity close to 85 dB is obtained in the three bands. A dispersion compensation system is set to preserve these performances as the imaging depth is varied. Compared

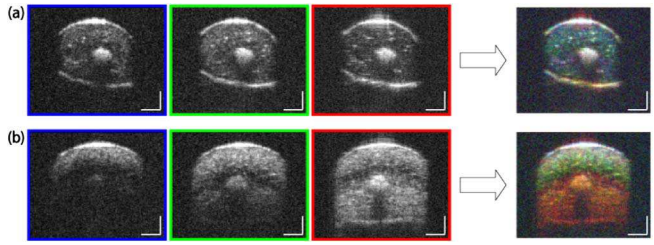

Fig. 6. xz sections of (a) a light and (b) a dark human hair. From left to right: in band 1, band 2, band 3, and with RGB representation. The scale bar is 20 μm in the two directions.

to conventional one-band imaging and even dual-band imaging, the technique provides image contrast enhancement and improved sample differentiation capability without significant loss of spatial resolution. Although three successive image acquisitions are required to produce a RGB image, unlike [7] and [9] one single camera and one single light source are employed, which make the system handier to use. Besides, this technological approach could be easily extended for imaging in more than three bands. This would provide real spectroscopic analysis of the imaged sample at the price of longer acquisition time and trade-off between spectral resolution and spatial resolution.

The authors wish to acknowledge the Agence Nationale de la Recherche and the European network for biophotonics “Photonics4Life.” They are grateful to Guillaume Dupuis at “Centre de Photonique Biomédicale” for providing gold beads.

References

1. L. Vabre, A. Dubois, and A. C. Boccara, Opt. Lett. **27**, 530 (2002).
2. B. Laude, A. De Martino, B. Drevillon, L. Benattar, and L. Schwartz, Appl. Opt. **41**, 6637 (2002).
3. A. Dubois, G. Moneron, K. Grieve, and A. C. Boccara, Phys. Med. Biol. **49**, 1227 (2004).
4. A. Dubois, J. Moreau, and C. Boccara, Opt. Express **16**, 17082 (2008).
5. U. Morgner, W. Drexler, F. X. Kartner, X. D. Li, C. Pitris, E. P. Ippen, and J. G. Fujimoto, Opt. Lett. **25**, 111 (2000).
6. C. Y. Xu, C. Vinegoni, T. S. Ralston, W. Luo, W. Tan, and S. A. Boppart, Opt. Lett. **31**, 1079 (2006).
7. D. Sacchet, J. Moreau, P. Georges, and A. Dubois, Opt. Express **16**, 19434 (2008).
8. F. Spoler, S. Kray, P. Grychtol, B. Hermes, J. Bornemann, M. Forst, and H. Kurz, Opt. Express **15**, 10832 (2007).
9. L. F. Yu and M. K. Kim, Opt. Express **12**, 6632 (2004).
10. A. Dubois, L. Vabre, A. C. Boccara, and E. Beaurepaire, Appl. Opt. **41**, 805 (2002).
11. A. Dubois, G. Moneron, and C. Boccara, Opt. Commun. **266**, 738 (2006).
12. I. H. Malitson, J. Opt. Soc. Am. **55**, 1205 (1965).
13. H. Liang, R. Lange, B. Peric, and M. Spring, Appl. Phys. B **26**, 1 (2013).
14. C. R. Simpson, M. Kohl, M. Essenpreis, and M. Cope, Phys. Med. Biol. **43**, 2465 (1998).